NIR-II luminescence and X-ray induced UV luminescence from Ce^{3+}, Nd^{3+} co-doped $NaLuF_4$ phosphors

Xiaodan Wang [a,b], Penghui Li [a,b], Shenghui Zheng [a,b], Junpeng Shi [c], Xiaoyan Fu [d,*], Hongwu Zhang [a,e,**]

[a] Key Laboratory of Urban Pollutant Conversion, Institute of Urban Environment, Chinese Academy of Sciences, Xiamen 361021, China
[b] University of Chinese Academy of Sciences, No. 19A Yuquan Road, Beijing 100049, China
[c] Key Laboratory of Design and Assembly of Functional Nanostructures, Fujian Institute of Research on the Structure of Matter, Chinese Academy of Sciences, Fuzhou 350002, China
[d] College of Materials Science and Engineering, Key Laboratory of Functional Materials and Applications of Fujian Province, Xiamen University of Technology, Xiamen 361024, China
[e] School of Chemistry and Material Sciences, Ludong University, Yantai 264025, China

ARTICLE INFO

ABSTRACT

Owning to exceptional optical and physicochemical properties, lanthanide-doped inorganic dual-mode luminescence materials are regarded as promising platform for multifunctional applications. Herein, a facile hydrothermal method is used to integrate Ce^{3+} and Nd^{3+} ions co-doped $NaLuF_4$ phosphors, achieving dual-mode with ultraviolet (UV) and the second near-infrared (NIR-II) luminescence from single particles under two excitation sources. Higher $NaF/LnCl_3$ ratio can not only promote the crystal phase transformation from cubic to hexagonal and the shape evolution from nanoparticles to microprisms, but also promote the UV and NIR-II luminescence properties of $NaLuF_4:Ce^{3+}$, Nd^{3+} phosphors. Upon irradiation with X-ray, Ce^{3+} and Nd^{3+} ions co-doped $NaLuF_4$ phosphors exhibit strong broad band UV emission due to 5d→4f transition emission of Ce^{3+}. Under 808 nm NIR excitation, the phosphors give NIR-II emission with two peaks at around 1060 nm and 1340 nm, which are attributed to the $^4F_{3/2}{\rightarrow}^4I_{11/2}$ and $^4F_{3/2}{\rightarrow}^4I_{13/2}$ electron transitions of Nd^{3+} ions respectively. Furthermore, the possible emission and energy transfer mechanism between Ce^{3+} and Nd^{3+} under the excitation of X-ray and 808 nm laser are discussed in details. The above results not only pave the way for future research of dual-mode luminescent materials, but also endow such materials with potential bio-applications for deep tissue bioimaging and therapy.

© 2020 Elsevier B.V. All rights reserved.

1. Introduction

In recent years, the dual-mode luminescence multifunctional materials have attracted tremendous attention due to their potential applications in various fields such as anti-counterfeiting, displaying, solid state laser, solar cells, biomedicines and light emitting diodes (LED) [1–4]. The dual-mode luminescence host materials include phosphates, vanadates, borates, and fluorides. For example, some groups studied the dual-mode luminescence of the Yb^{3+} and Tb^{3+} ions co-doped YPO_4 nanocrystals [5] and YBO_3 materials [6], the Yb^{3+} and Ho^{3+} ions co-doped YVO_4 nanoparticles [7] and the dual-mode emission of $NaGdF_4:Yb/Tm@NaGdF_4:Ce/Tb$ nanoarchitecture [8]. Among them, rare earth fluorides ($NaLnF_4$) with low phonon energy, high chemical stabilities and high refractive index are considered as excellent down-conversion (DC) and up-conversion (UC) luminescence host materials for lanthanide ions due to their large Stokes shifts, sharp emission peaks, widely tunable emission colors, high photostability and low toxicity [9]. According to previous literature reports, $NaLuF_4$ have been known as one of the most excellent host materials due to a unique electronic state at the top of the valence band and a smaller unit-cell volume [10–12]. Furthermore, Lu based host ($NaLuF_4$) has large X-ray absorption coefficients, K-edge values and the largest atomic number, making it ideal contrast agent for X-ray computed tomography imaging [13].

It is well known that the emission of lanthanide-doped materials originates primarily from the electronic transitions within the unique $4f^N$ configurations (N=0–14) of trivalent lanthanide ions (Ln^{3+}) [14,15]. Different lanthanide dopants produce different emission

* Corresponding author.
** Corresponding author at: Key Laboratory of Urban Pollutant Conversion, Institute of Urban Environment, Chinese Academy of Sciences, Xiamen 361021, China.
E-mail addresses: fuxiaoyan@xmut.edu.cn (X. Fu), hwzhang@iue.ac.cn (H. Zhang).

patterns under irradiation sources. Through judicious selection of lanthanide ions embedded in an appropriate inorganic host lattice, the luminescent properties, such as emission color from ultraviolet, visible to NIR and luminescent intensity, can be accurately controlled due to the rich energy levels of Ln^{3+}. As they can be tuned from the UV to the NIR region, lanthanide-doped luminescence materials have attracted great research for potential bioapplications including bioimaging, detection, as well as disease diagnosis and therapy [16–19].

Recently, the trivalent Ln^{3+} ions such as Ce^{3+}, and Nd^{3+} with unique properties are widely concerned by the researches. For instance, Ce^{3+} ions serve not only as the great sensitizer to enhance the emission intensity Ln^{3+} ions, but also as an excellent luminescent center to show a broad UV emission band due to its 5d to 4f transition emission [20,21]. Ultraviolet radiation spans the range of wavelengths between 200 and 400 nm and can be divided into three groups: ultraviolet C (UVC, 200–280 nm), ultraviolet B (UVB, 280–320 nm), ultraviolet A (UVA, 320–400 nm). Many researches have confirmed that UV photons are able to inactivate cells due to their direct interaction with DNA, causing a variety of forms of damage, and have been extensively used in medical applications such as sterilization and disinfection, treatment of psoriasis, photodynamic therapy [22–24]. However, commonly used UV lamps or lasers have major drawbacks, such as severe phototoxicity and significantly limited tissue penetrability. Owing to the excellent penetration ability, X-rays hold the potential to become an ideal energy source to excite the luminescence centers and are widely used in clinical cancer diagnosis and therapy in deep tissue without considering the energy loss [25]. Thus, an in-situ generation of UV light utilizing particles with a low-energy X-ray excitation is quite desirable. Ce doped phosphors are able to convert X-ray energy into UV photons, thus achieving deep penetration into tissue. For example, Clement et al. reported the CeF_3 nanoparticles conjugated with the photosensitizer verteporfin through electrostatic interaction. Upon 8 keV X-ray radiation, CeF_3 emits UV light, which in turn, excited verteporfin and leaded to singlet oxygen generation, which enhanced cell killing and supplements the ionizing radiation and photodynamic treatments of cancer [26]. Zhang et al. reported the downconverted UV fluorescence from Ce-doped $LiYF_4$ nanoscintillator under X-ray induced irradiation enabled the generation of electron–hole pairs in ZnO nanoparticles and the formation of biotoxic hydroxyl radicals, achieving synchronous radiotherapy and ionizing-radiation-induced deep PDT [27]. Du et al. reported that Ce-doped $LiLuF_4$ not only can act as radiosensitizers for enhancing the yield of ROS including $O_2^{-\bullet}$ under X-ray irradiation, but also could convert X-ray into UV light to activate the photoactive RBS to release NO for effective theranostic agents in cancer radiotherapy [28]. Besides, Nd^{3+} is particularly interesting among Ln^{3+} ions for bioimaging due to its excitation light of 808 nm and intrinsic NIR emissive luminescent properties [29]. First of all, it can be efficiently excited with 808 nm radiation, which lies in the first biological window and has been also demonstrated to be a non-heating, non-damaging wavelength in biological applications that can be produced by cost- effective laser diode. Moreover, Nd^{3+} ions present down conversion NIR-II emission bands (at around 1060 and 1340 nm), all lie in the second biological windows, which exhibit enhanced deep-tissue imaging capability using an infrared camera. Up to now, there are some groups that have synthesized the Ce^{3+} ions doped $NaLuF_4$ and Nd^{3+} ions doped $NaLuF_4$ [30–32]. However, as far as we all know, the dual mode luminescence behavior of Ce^{3+}, Nd^{3+} ions co-doped $NaLuF_4$ phosphors have not been investigated. With the combined favorable properties that arise from lanthanide doping, multifunctional materials for various bio-applications may be achieved.

The main goal of the current paper is the evaluation of the physico-chemical properties of $NaLuF_4$ phosphors activated with Ce^{3+} and Nd^{3+} ions, with special emphasis on the dual-mode luminescence properties of the obtained system. In this work, Ce^{3+} and Nd^{3+} ions co-doped $NaLuF_4$ phosphors were prepared by hydrothermal method. The effects of $NaF/LnCl_3$ ratio on the phase compositions, morphologies, size and luminescence properties of $NaLuF_4$:Ce^{3+}, Nd^{3+} crystals were investigated in detail. Selecting Ce^{3+} and Nd^{3+} as activators can simultaneously show UV and NIR-II emission under X-ray and 808 nm laser excitation. Corresponding energy transfer mechanism under different excitation sources was also proposed. These single-particle phosphors with dual-mode emission would have potential applications in many fields such as deep tissue bioimaging and therapy.

2. Experiment section

2.1. Chemicals and materials

Lutetium chloride hexahydrate ($LuCl_3 \cdot 6H_2O$, 99.99%), neodymium chloride hexahydrate ($NdCl_3 \cdot 6H_2O$, 99.9%), and cerium chloride hexahydrate ($CeCl_3 \cdot 6H_2O$, 99.99%) were purchased from Aladdin (Shanghai, China). Oleic acid (OA), NaOH, NaF (98%) and ethanol were supplied from Sinopharm Chemical Reagent Co., Ltd. (Shanghai, China). All the chemicals were of analytical grade and used without further purification.

2.2. Preparation of OA-coated $NaLuF_4$: Ce^{3+}, Nd^{3+} samples

OA-coated $NaLuF_4$:xCe^{3+}, yNd^{3+} (x=0-0.07, y=0-0.05)(x=0–0.07, y=0–0.05) samples were synthesized via hydrothermal method using oleic acid as a stabilizing agent. In a typical procedure, 10 mL of ethanol was added to 3 mL of an aqueous solution containing 0.6 g of NaOH under stirring to form a homogeneous solution. Then, 14 mL of oleic acid was added to the above solution to yield a viscous solution. After vigorously stirred for 20 min, 1 mmol $RECl_3$ (RE=Lu, Ce, and Nd with at designed molar ratios) was added into the above solution and kept vigorous stirring. After agitating for 30 min, 4 mL (4 mmol) of aqueous NaF solutions (1.0 M) were added. The mixed solution was agitated for 30 min, then transferred into a 50 mL stainless Teflon-lined autoclave, sealed and heated at 200 °C for 24 h. After reaction, the system was cooled naturally to room temperature and the products were deposited at the bottom of the container. The as-prepared samples were separated by centrifugation, washed several times with ethanol and dried at 60 °C for 12 h. Different NaF contents (2, 3, 3.5, 5 mmol) were employed to study the effects on the phase structure, morphology, and particle size of the $NaLuF_4$:Ce^{3+}, Nd^{3+} samples by similar procedure as described above.

2.3. Characterization

The crystal structure of the samples was measured using X-ray diffraction (PANalytical, Netherlands) at 40 kV and 40 mA with Cu Kα radiation (λ=1.5406 Å) and the date were collected in the 2θ range from 10° to 80°. The morphology and elemental mapping of the $NaLuF_4$:Ce^{3+}, Nd^{3+} samples were measured by transmission electron microscopy scanning (TEM, JEOL, JEM-2100, Japan) and electron microscopy (SEM, S-4800, Hitachi, Japan) equipped with energy-dispersive X-ray spectrometer (EDS) detection function. The NIR fluorescence spectrum was measured by using the FLS920 fluorescence spectrometer (Edinburgh, UK), equipped with an external 808 nm diode laser (500 mW power) as the excitation source at room temperature. And the X-ray excited radioluminescence spectra were recorded using fiber optic cables connected to the FLS920 fluorescence spectrometer. An X-ray tube operated at 50 kV and 80 μA has been used for the X-ray excitation.

3. Results and discussion

3.1. Crystal structure of NaLuF$_4$:Ce^{3+}, Nd^{3+}

The crystal structure of NaLuF$_4$ has two forms of the cubic (α-) and the hexagonal (β-) phase. α-NaLuF$_4$ nanocrystals and β-NaLuF$_4$ microcrystals can be obtained by simply adding different NaF contents into the initial solution. The XRD patterns of NaLuF$_4$:Ce^{3+}, Nd^{3+} crystals with different molar ratios of NaF/LnCl$_3$ at 200 °C for 24 h are shown in Fig. 1(a). The sample exhibits pure cubic phase (JCPDS No. 27-0725) when the NaF/LnCl$_3$ ratio is below 3:1. when the molar ratio of NaF/LnCl$_3$ is fixed at 3.5:1, β-NaLuF$_4$ phase emerges in addition to the α-NaLuF$_4$ phase, indicating that the sample partially transforms from cubic to hexagonal phase. With the NaF/LnCl$_3$ ratio further increases to 4:1 and 5:1, pure hexagonal phase NaLuF$_4$:Ce^{3+}/ Nd^{3+} crystals are obtained. In addition, as the NaF/LnCl$_3$ ratio is enhanced to 5:1, small amounts of NaF were found in the XRD patterns of the samples. The results indicate that larger NaF/LnCl$_3$ ratio is benefit for the formation of hexagonal phase NaLuF$_4$. The XRD patterns of the hexagonal phase NaLuF$_4$:Ce^{3+}, Nd^{3+} (NaF/ LnCl$_3$=4:1) with different Ce^{3+}, Nd^{3+} concentrations are shown in Fig. 1(b). All the diffraction peaks are in good agreement with reference data of hexagonal NaLuF$_4$ (JCPDS No. 27-0726). Notably, no other diffraction peaks are detected, indicating the formation of the pure hexagonal phase crystals. In addition, it is noticed that the diffraction peaks exhibit a slight shift towards a lower angle with respect to those of NaLuF$_4$ in the JCPDS card due to the substitution by Ce^{3+} and Nd^{3+} with larger ionic radius than that of Lu^{3+} in the host lattice, which indicates that Ce^{3+} and Nd^{3+} ions are incorporated in the lattice by substituting the Lu^{3+} sites.

To further verify the phase and detailed structure, the as-prepared NaLuF$_4$:0.05Ce^{3+}, 0.02Nd^{3+} particles with different molar ratios of NaF/LnCl$_3$ were characterized by TEM and SEM. Fig. 2(a) and (b) show the TEM images of α-NaLuF$_4$:0.05Ce^{3+}, 0.02Nd^{3+} crystals prepared with the NaF/LnCl$_3$ ratio of 2:1 and 3:1, which are sphere-like structure with an average size of about 20 nm. With the NaF/ LnCl$_3$ ratio increases to 3.5:1, the corresponding TEM image (Fig. 2c) exhibits two distinct particle morphologies including small nanoparticles and larger microprisms. As the NaF/LnCl$_3$ ratio increases to

4:1(Fig. 2d), short hexagonal phase microprisms with average size of 1.64 μm in diameter and 0.67 μm in thickness are achieved. Further increasing the NaF/LnCl$_3$ ratio to 5:1, the as prepared samples present long hexagonal microprisms with average size of 1.44 μm in diameter and 1.97 μm in thickness further growing along the axial direction in Fig. 2(e). These results are in good agreement with the XRD results. These elementary results indicated that the NaF content has a great effect on the morphology and size of the as synthesized crystals. To confirm the elemental composition, energy dispersive X-ray spectra (EDS), and elemental mapping were performed. EDS analysis illustrated in Fig. 2(f) verified the element composition of Na, F, Lu, Ce, and Nd, indicating the Ce and Nd were successfully doped into the host matrix. In addition, EDS elemental mapping results further revealed that the elements including Na, F, Lu, Ce, and Nd were evenly distributed over the particles, as presented in Fig. 2(g)–(l).

3.2. Luminescence properties of α-NaLuF$_4$ and β-NaLuF$_4$ crystals

We selected α-NaLuF$_4$:0.05Ce^{3+}, 0.02Nd^{3+} nanoparticles prepared at NaF/LnCl$_3$=3:1 and β-NaLuF$_4$:0.05Ce^{3+}, 0.02Nd^{3+} microprisms prepared at NaF/LnCl$_3$=4:1 to investigate the luminescence properties of α-NaLuF$_4$ and β-NaLuF$_4$ crystals. X-ray excited luminescence spectra and the NIR-II emission spectra of NaLuF$_4$:0.05Ce^{3+}, 0.02Nd^{3+} crystals with different molar ratios of NaF/LnCl$_3$ are presented in Fig. 3. We can see from spectral analysis that the UV and NIR-II luminescence intensities of β-NaLuF$_4$:0.05Ce^{3+}, 0.02Nd^{3+} microprisms were much stronger than that of α-NaLuF$_4$:0.05Ce^{3+}, 0.02Nd^{3+} nanoparticles. As the physical dimension of the particles is reduced, high surface tension triggers phase transformation from hexagonal to cubic, resulting in a significant decrease of luminescence. It is known that the luminescence efficiency of hexagonal NaLnF$_4$ crystals is much higher than that of the cubic phase [33]. Therefore, it is very important to study the effect of the hexagonal phase structure on the luminescence properties of rare earth doped NaLuF$_4$ crystals.

3.3. UV luminescence properties of NaLuF$_4$:Ce^{3+}, Nd^{3+} Microprisms

The X-ray excited luminescence spectra of pure NaLuF$_4$ and NaLuF$_4$:0.05Ce^{3+} phosphors (Fig. 4a) and NaLuF$_4$: 0.02Nd^{3+}, xCe^{3+} (x=0,
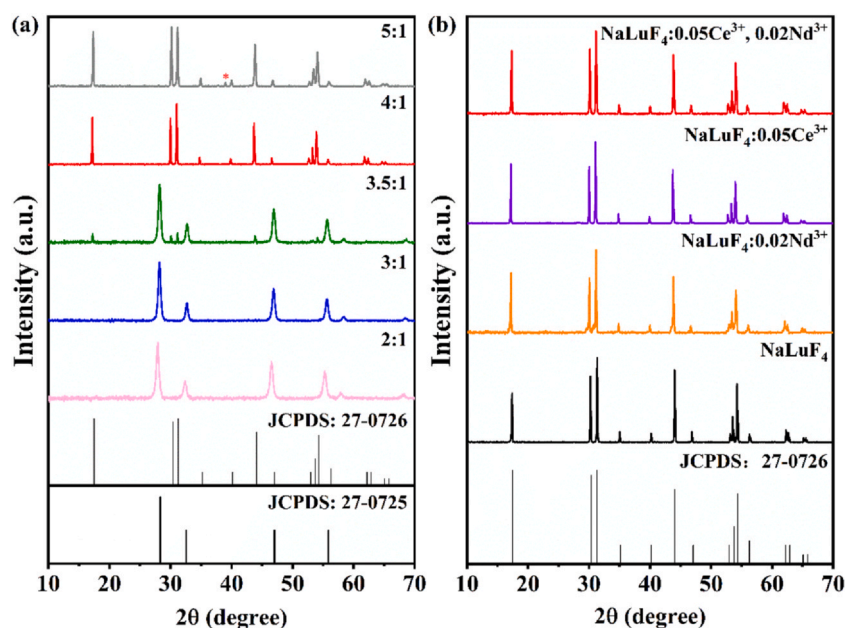

Fig. 1. The XRD diffraction patterns of (a) NaLuF$_4$:Nd^{3+}, Ce^{3+} crystals synthesized with different molar ratios of NaF/LnCl$_3$, and (b) NaLuF$_4$:xCe^{3+}, yNd^{3+} samples prepared at NaF/ LnCl$_3$=4:1. The peak marked by asterisk (*) arises from excessive cubic NaF.
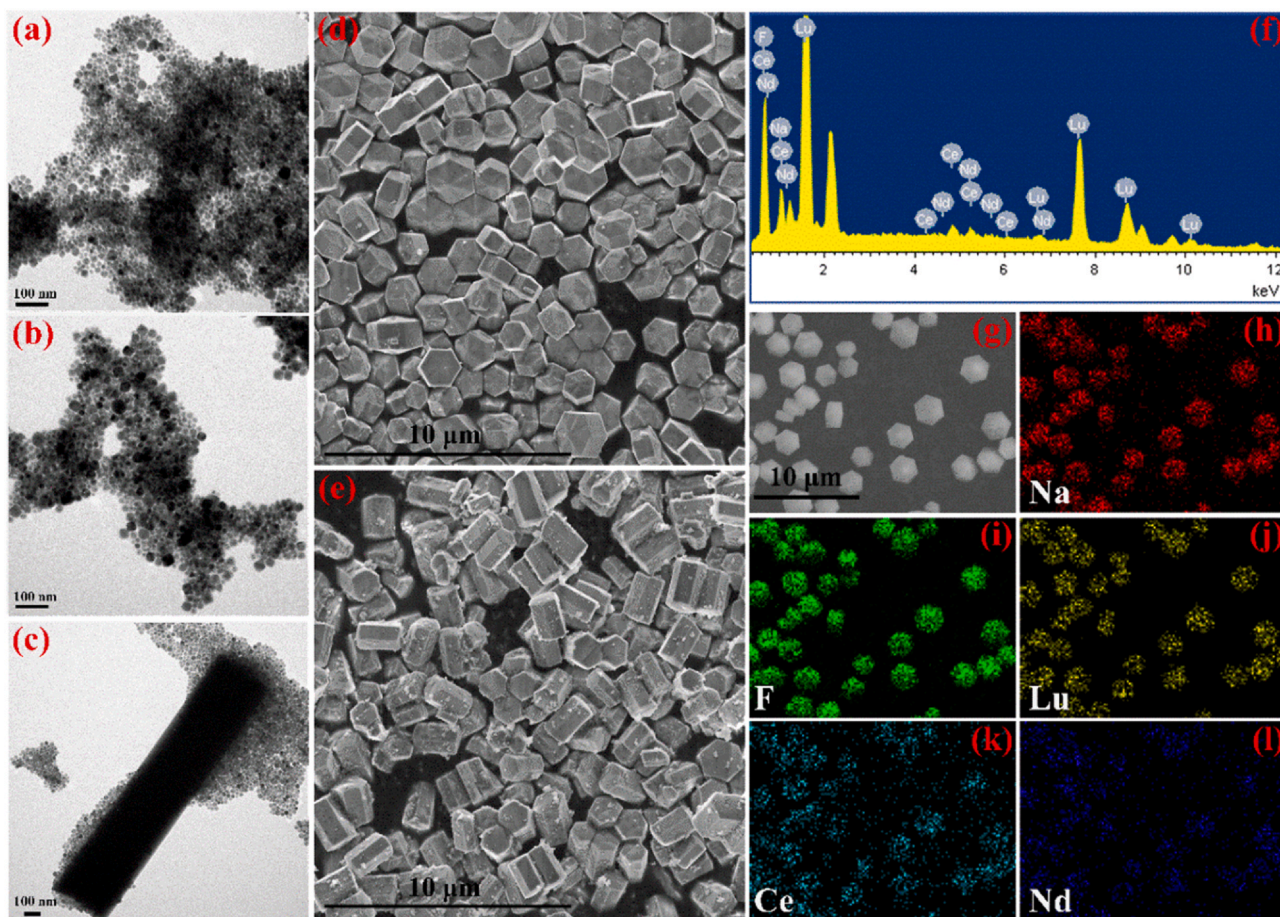
Fig. 2. TEM images of NaLuF$_4$:Nd^{3+}, Ce^{3+} samples with molar ratio of NaF/LnCl$_3$ = (a) 2:1; (b) 3:1; (c) 3.5:1. SEM images of NaLuF$_4$:Nd^{3+}, Ce^{3+} samples with molar ratio of NaF/LnCl$_3$ = (d) 4:1; (e) 5:1. (f) EDS pattern of the β-NaLuF4:0.05Ce^{3+}, 0.02Nd^{3+} prepared at NaF/LnCl$_3$ = 4:1. SEM image of (g) the β-NaLuF$_4$:0.05Ce^{3+}, 0.02Nd^{3+}, and the corresponding elemental mapping images for (h) Na, (i) F, (j) Lu, (k) Ce and (l) Nd.
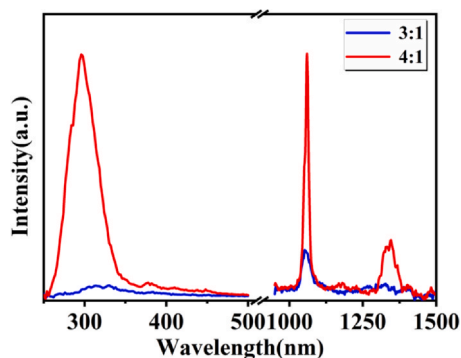

Fig. 3. X-ray excited luminescence spectra and the NIR-II emission spectra of NaLuF$_4$:0.05 Ce^{3+}, 0.02 Nd^{3+} crystals with molar ratio of NaF/LnCl$_3$=3:1 and 4:1 after excitation with an X-ray source at ~80 kV and 5 µA and the excitation of 808 nm laser (500 mW power).

Fig. 4. X-ray excited luminescence spectra of (a) NaLuF$_4$ undoped and doped Ce^{3+}; and (b) NaLuF$_4$:0.02 Nd^{3+}, x Ce^{3+} samples with x=0, 0.01, 0.03, 0. 05, and 0.07 after excitation with an X-ray source at ~80 kV and 5 µA; Insets are the strongest emission intensity of Ce^{3+} in the as-synthesized samples as a function of Ce^{3+}ions concentration upon X-ray excitation. All the samples were prepared at NaF/LnCl$_3$= 4:1.

0.01, 0.03, 0.05 and 0.07) (Fig. 4b) were examined at room temperature. Under X-ray irradiation, the pure host of NaLuF$_4$ didn't show any obvious emission, while the Ce doped phosphor exhibited an intense broad emission band in the range of 250–350 nm peaking at about 298 nm, predominantly in the high-energy UVB spectral region. The dominant UV emission portion is attributed to the 5d→4f transition of Ce^{3+}. Considering that the X-ray mass absorption coefficient of lutetium
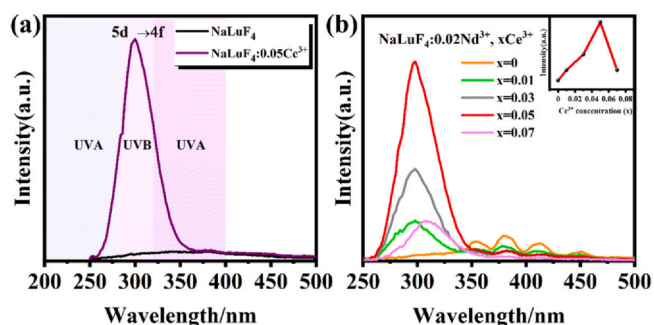
is high, it could absorb energy from the X-ray and transfer to the luminescent center more efficiently. The luminescent measurements demonstrated that pure NaLuF$_4$ is an effective host to transfer the high energy of X-ray to Ce^{3+} ions as the luminescence centers, but can't act as a scintillator by its intrinsic transition. Furthermore, we investigated the relationship between the amount of Ce^{3+} doping and the UV luminescence intensities to determine the optimal doping
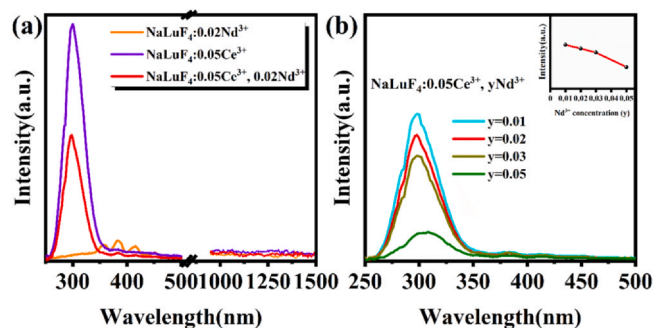
Fig. 5. X-ray excited luminescence spectra of (a) Ce^{3+} doped, Nd^{3+} doped and Ce^{3+}-Nd^{3+} co-doped $NaLuF_4$; and (b)$NaLuF_4$:0.05 Ce^{3+}, yNd^{3+}samples with y = 0.01, 0.02, 0.03, and 0.05 after excitation with an X-ray source at ~80 kV and 5 μA; Insets are the strongest emission intensity of Ce^{3+} as a function of Nd^{3+} ions concentration upon X-ray excitation. All the samples were prepared at $NaF/LnCl_3$=4:1.

Fig. 6. The NIR-II emission spectra of (a) $NaLuF_4$ undoped and doped Nd^{3+}, and (b) $NaLuF_4$:0.05Ce^{3+}, yNd^{3+} samples with y=0, 0.01, 0.02, 0.03, and 0.05 under the excitation of 808 nm laser (500 mW power) at room temperature; Insets are the emission intensities of Nd^{3+} (1060 nm) in the as-synthesized samples as a function of Nd^{3+} ions concentration upon 808 nm laser irradiation. All the samples were prepared at $NaF/LnCl_3$ = 4:1.

concentrations. With increasing Ce^{3+} doping concentration, the UV luminescence intensities increased gradually and then reached to the maximum at x = 0.05 and then decreased because of concentration quenching effect, which could be ascribed to the cross relaxation between neighboring Ce^{3+} ions, as shown in the inset of Fig. 4(b)..

Fig. 5(a) illustrates the emission spectra of the $NaLuF_4$:0.02Nd^{3+}, $NaLuF_4$:0.05Ce^{3+} and $NaLuF_4$:0.05Ce^{3+}, 0.02Nd^{3+} products under X-ray excitation. The emission spectrum of the Nd^{3+} single doped samples exhibited some weak emission peaks at around 350 nm, 380 nm, 410 nm, and 450 nm corresponding to the $^4D_{3/2} \rightarrow {}^4I_J$ transitions of Nd^{3+} ions under the X-rays excitation [20,34]. With Ce^{3+} and Nd^{3+} co-doping, the UV emission band from 5d→4f was detected in the UV spectral regions, while the small emission peaks of Nd^{3+} ions were not observed. Besides, we can also find that the main emission intensity ($^4D_{3/2} \rightarrow {}^4I_J$) of Nd^{3+} ions gradually decreases with an increase in the amount of Ce^{3+} ions and is almost undetectable finally when the Ce^{3+} concentration is higher than 0.05 (see Fig. 4b). A possible explanation for this phenomenon is that Nd^{3+} ions and Ce^{3+} ions in the double-doped system are competitive in absorbing the high X-ray energy to yield the emission of numerous lower energy photons. Compared with Ce^{3+} ions, Nd^{3+} ions have relatively weak absorption of excitation energy. The X-ray energy absorbed by the $NaLuF_4$:Ce^{3+}, Nd^{3+} samples is transferred to Ce^{3+} ions rather than Nd^{3+} ions, so Nd^{3+} ions cannot get more energy, which leads to its luminescence attenuation. And additionally, the UV emission intensity of Ce^{3+} and Nd^{3+} ions co-doped $NaLuF_4$ was significantly weaker than that of Ce^{3+} single doped $NaLuF_4$ shown in the Fig. 5(a). The above phenomenon evidently demonstrated that the introduction of Nd^{3+} ions effects the UV emission of Ce^{3+} ions. To further reveal the effect of Nd^{3+} ions content on the UV emission, we investigated the emission spectra of Ce^{3+} and Nd^{3+} ions co-doped $NaLuF_4$ phosphors by fixing the doped concentration of Ce^{3+} ions at 0.05 and changing the doped concentrations of Nd^{3+} ions from 0.01 to 0.05. From the inset of Fig. 5(b), it is clearly seen that emission intensities of Ce^{3+} ions are sensitive to the presence of Nd^{3+} co-dopants. The UV emission intensity of Ce^{3+} was gradually decreasing with increasing Nd^{3+} concentrations which may be induced by the concentration quenching effect. It is found that the distances among lanthanide ions will change with lanthanide ions doping in host materials [35]. Therefore, when increasing the concentration of Nd^{3+} ions, the distances between the Ce^{3+}-Ce^{3+} ions become shorter, resulting in stronger interactions and cross relaxation between Ce^{3+} ions. Finally, the UV luminescence emission intensity becomes weaker. Upon X-ray irradiation, Ce^{3+} and Nd^{3+} ions co-doped $NaLuF_4$ phosphors can convert X-ray photons to UV light that matches well with the absorption band of a range of photosensitizers, such as titanium dioxide (TiO_2) [24,36] and ZnO nanoparticles [27,37], which enables them to be potentially applied in deep-seated photodynamic therapy.
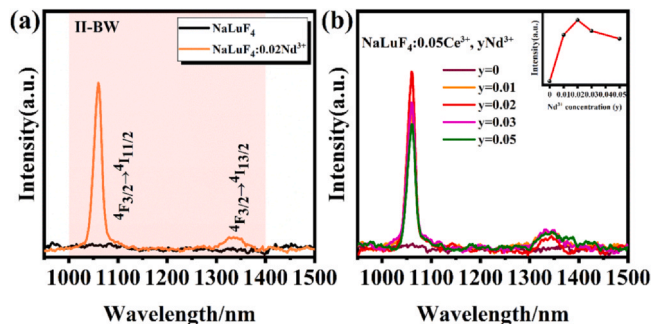
3.4. NIR-II luminescence properties of $NaLuF_4$: Ce^{3+}, Nd^{3+} Microprisms

Fig. 6(a) exhibits the emission spectra of pure $NaLuF_4$ and $NaLuF_4$: Nd^{3+} phosphors at room temperature. Under excited at 808 nm diode laser (500 mW cm^{-2}), the pure host of $NaLuF_4$ didn't show any obvious emission, while the Nd doped phosphors exhibited two main NIR-II emission bands located at around 1060 and 1340 nm, which were attributed to the $^4F_{3/2}$-$^4I_{11/2}$ and $^4F_{3/2}$-$^4I_{13/2}$ electron transitions of Nd^{3+} ions respectively. The results also indicated that pure $NaLuF_4$ could be an effective host to transfer the energy to Nd^{3+} ions as the luminescence centers. In order to select the optimum Nd^{3+} doping concentration in NIR-II luminescence, the emission properties of the as-prepared $NaLuF_4$:0.05Ce^{3+}, Nd^{3+} samples with different Nd^{3+} concentrations were investigated under the same experimental conditions. As shown in Fig. 6(b), following the increase of Nd^{3+} concentration from 0.01 to 0.02, the intensity of NIR-II emission increased. However, after reaching the maximum emission intensity at y=0.02 (inset in Fig. 6b), it gradually decreased with higher Nd^{3+} concentrations. The enhancement of NIR-II emission intensity induced by Nd^{3+} doping is mainly attributed to the efficient energy transfer between the decreased distances of the adjacent Nd^{3+}, while the decrease of emission intensity at high doping level may be ascribed to the severe cross relaxation among neighboring Nd^{3+} ions.

Fig. 7(a) illustrates the NIR-II emission spectra of the $NaLuF_4$:0.02Nd^{3+}, $NaLuF_4$:0.05Ce^{3+} and $NaLuF_4$:0.05Ce^{3+}, 0.02Nd^{3+} samples under the irradiation of 808 nm laser. The Ce^{3+} single doped samples didn't display any obvious emission spectrum in the near infrared region.
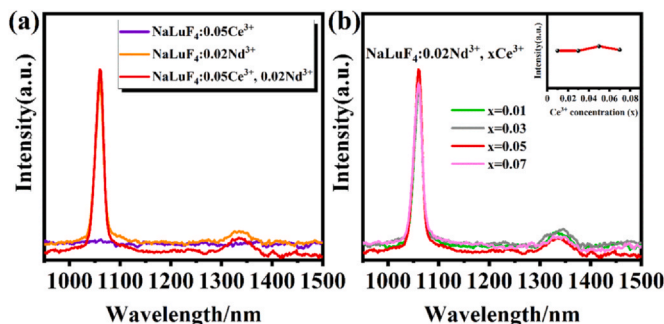

Fig. 7. The NIR-II emission spectra of (a) Ce^{3+} doped, Nd^{3+} doped and Ce^{3+}-Nd^{3+} co-doped $NaLuF_4$, and (b) $NaLuF_4$:0.02Nd^{3+}, xCe^{3+} samples with x=0.01, 0.03, 0.05, and 0.07 under the excitation of 808 nm laser (500 mW power) at room temperature; Insets are the 1060 nm emission intensity of Nd^{3+} as a function of Ce^{3+} ions concentration upon 808 nm laser irradiation. All the samples were prepared at $NaF/LnCl_3$=4:1.
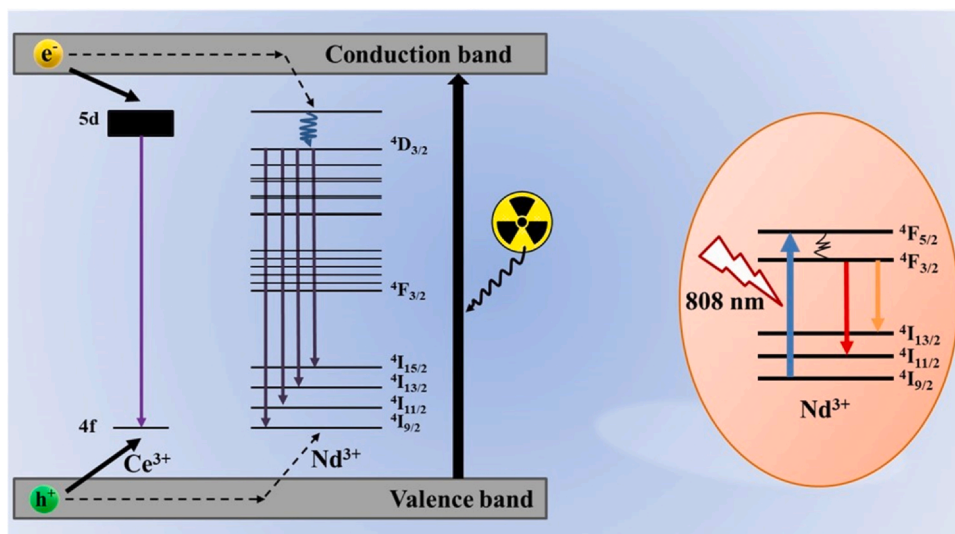
Fig. 8. Schematic energy-level diagram of Nd^{3+} and Ce^{3+} in $NaLuF_4$ as well as the UV and NIR-II emission mechanisms under the excitation of X-ray and 808 nm laser.

With Ce^{3+} and Nd^{3+} co-doping $NaLuF_4$ phosphors, the NIR-II emission intensity was slightly higher than that of the single doped Nd^{3+} ions. To reveal the effect of Ce^{3+} content on the NIR-II emission, NIR emission properties of the $NaLuF_4$:Ce^{3+}, $0.02Nd^{3+}$ samples doped with different concentrations of Ce^{3+} (0.01, 0.03, 0.05, 0.07) were further studied under the excitation of 808 nm laser, as demonstrated in Fig. 7(b). Obviously, with the increase of Ce^{3+} concentrations and fixed Nd^{3+} concentration, the intensities of NIR-II emission at 1060 nm have changed little. Therefore, all the results confirmed that the introducing of Ce^{3+} dopants has little effect on the NIR-II luminescence of Nd^{3+}. These observations imply that there is no energy transfer between Ce^{3+} ions and Nd^{3+} ions under the 808 nm laser excitation.

Since the excitation of 808 nm lies in the first biological window (700–1000 nm) and the strongest emission wavelength at 1060 nm belongs to the second biological window (II-BW) (1000–1400 nm), $NaLuF_4$:Ce^{3+}, Nd^{3+} samples have great potential as an optical imaging agent for deep tissue imaging with deeper light penetration and high contrast imaging.

3.5. Energy transfer mechanism

Based on all these observations, we propose a plausible mechanism for the UV and NIR-II luminescence of Ce^{3+}-Nd^{3+} co-doped $NaLuF_4$ under different excitation source, as schematized in Fig. 8. Upon X-ray irradiation, the absorption of an X-ray photon yields an energetic, ionized free electron. This hot electron collides with atoms in the material, and it triggers the cascading production of additional ionized electrons. Lower-energy collisions may cause the excitation of valence band electrons into the conduction band, leading to the formation of many electron–hole pairs. The thermalized electrons and created holes are subsequently captured by Nd^{3+} and Ce^{3+} ions, respectively. Via relaxation process such as radiative pathway or heat dissipation, the excitation energy can migrate to the Ce^{3+} giving rise to the 5d→4f emission, or it can transfer to the Nd^{3+} in the form of the $^4D_{3/2}$→^4I_J emission. The simple competition between Ce^{3+} and Nd^{3+} for excitation energy can take place as a parallel process. Under the excitation of 808 nm laser, the Ce^{3+} ions don't show any emission peak in the NIR region, while the Nd^{3+} ions are excited from $^4I_{9/2}$ to $^4F_{5/2}$, and then the electron from the excited state relaxes to $^4F_{3/2}$ nonradiatively. Finally, recombination of Nd^{3+} occurs from $^4F_{3/2}$ to ^4I_J (J = 11/2, 13/2) and gives out the corresponding NIR-II emissions at around 1060

and 1340 nm, respectively. Energy transfer seems to work from Ce^{3+} to Nd^{3+} ion under different excitation conditions.

4. Conclusions

In summary, Ce^{3+} and Nd^{3+} ions co-doped $NaLuF_4$ phosphors have been successfully synthesized through a simple hydrothermal method in order to achieve efficient and dual-mode emissions at single-particle levels under different excitation conditions. It is found that with the larger $NaF/LnCl_3$ ratio, the phase of $NaLuF_4$:Ce^{3+}, Nd^{3+} transforms from cubic to hexagonal, and the morphology changes from nanoparticles to microprisms, which results in the sharp increase of UV and NIR-II emission intensity. Excitation by X-ray, which corresponds to the 4 f→5d transition in Ce^{3+} ions, causes all the Ce^{3+}-Nd^{3+} co-doped $NaLuF_4$ samples to show a broad UV emission due to the 5d→4 f transition of Ce^{3+} ions. On the other hand, excitation at 808 nm laser, which corresponds to the $^4I_{9/2}$ to $^4F_{5/2}$ transition in Nd^{3+} ions, causes all the Ce^{3+}-Nd^{3+} co-doped $NaLuF_4$ samples to generate NIR-II emissions due to the $^4F_{3/2}$ → $^4I_{11/2}$ and $^4F_{3/2}$ → $^4I_{13/2}$ electron transitions of Nd^{3+} ions. Furthermore, the energy transfer mechanism between Ce^{3+} and Nd^{3+} ions is proposed. As a result, by adjusting the dopant content of Ce^{3+} and Nd^{3+} ions in the host lattice, efficient dual-mode luminescence can be achieved in the co-doped $NaLuF_4$ microprisms through the dual-mode excitation strategy, which could provide potential insight for highly promising multifunctional applications such as deep tissue bioimaging and photodynamic therapy.

CRediT authorship contribution statement

Xiaodan Wang: Conceptualization, Methodology, Investigation, Formal analysis, Writing - original draft. **Penghui Li**: Resources, Visualization. **Shenghui Zheng**: Data Curation, Visualization. **Junpeng Shi**: Project administration, Funding acquisition. **Xiaoyan Fu**: Supervision, Funding acquisition. **Hongwu Zhang**: Validation, Writing - review & editing, Funding acquisition.

Declaration of Competing Interest

The authors declare that they have no known competing financial interests or personal relationships that could have appeared to influence the work reported in this paper.

Acknowledgements

References

[1] H. Huang, J. Chen, Y. Liu, J. Lin, S. Wang, F. Huang, D. Chen, Lanthanide-doped core@multishell nanoarchitectures: multimodal excitable upconverting/downshifting luminescence and high-level anti-counterfeiting, Small 16 (2020) 2000708.

[2] S.E. Seo, C.S. Park, S.J. Park, K.H. Kim, J. Lee, J. Kim, S.H. Lee, H.S. Song, T.H. Ha, J.-H. Kim, H.W. Yim, H.-I Kim, O.S. Kwon, Single-photon-driven up-/down-conversion nanohybrids for in vivo mercury detection and real-time tracking, J. Mater. Chem. A 8 (2020) 1668–1677.

[3] L. Xu, Y. Li, Q. Pan, D. Wang, S. Li, G. Wang, Y. Chen, P. Zhu, W. Qin, Dual-mode light-emitting lanthanide metal-organic frameworks with high water and thermal stability and their application in white LEDs, ACS Appl. Mater. Interfaces 12 (2020) 18934–18943.

[4] X. Xu, W. Li, W. Zhou, G. Tan, Y. Zheng, C. Hu, B. Lei, X. Zhang, Y. Liu, J. Zhuang, Preparation and properties of dual-mode luminescent NaYF$_4$:Yb,Tm@SiO$_2$/carbon dot nanocomposites, J. Mater. Chem. C 6 (2018) 10360–10366.

[5] T. Grzyb, R.J. Wiglusz, A. Gruszeczka, S. Lis, Down- and up-converting dual-mode YPO$_4$:Yb^{3+}, Tb^{3+} nanocrystals: synthesis and spectroscopic properties, Dalton Trans. 43 (2014) 17255–17264.

[6] T. Grzyb, K. Kubasiewicz, A. Szczeszak, S. Lis, Energy migration in YBO$_3$:Yb^{3+}, Tb^{3+} materials: down- and upconversion luminescence studies, J. Alloy. Compd. 686 (2016) 951–961.

[7] M. Kumar Mahata, T. Koppe, K. Kumar, H. Hofsass, U. Vetter, Demonstration of temperature dependent energy migration in dual-mode Ho^{3+}/Yb^{3+} nanocrystals for low temperature thermometry, Sci. Rep. 6 (2016) 36342.

[8] M. Ding, D. Chen, Z. Wan, Y. Zhou, J. Zhong, J. Xi, Z. Ji, Achieving efficient Tb^{3+} dual-mode luminescence via Gd-sublattice-mediated energy migration in a NaGdF$_4$ core-shell nanoarchitecture, J. Mater. Chem. C 3 (2015) 5372–5376.

[9] Q. Zhao, Z. Xu, Y. Sun, Rare earth fluoride nano-/microstructures: hydrothermal synthesis, luminescent properties and applications, J. Nanosci. Nanotechnol. 14 (2014) 1675–1692.

[10] S. Zeng, J. Xiao, Q. Yang, J. Hao, Bi-functional NaLuF$_4$:Gd^{3+}/Yb^{3+}/Tm^{3+} nanocrystals: structure controlled synthesis, near-infrared upconversion emission and tunable magnetic properties, J. Mater. Chem. 22 (2012) 9870–9874.

[11] Y. Li, J. Zhang, Y. Luo, X. Zhang, Z. Hao, X. Wang, Color control and white light generation of upconversion luminescence by operating dopant concentrations and pump densities in Yb^{3+}, Er^{3+} and Tm^{3+} tri-doped Lu$_2$O$_3$ nanocrystals, J. Mater. Chem. 21 (2011) 2895–2900.

[12] J. Ouyang, D. Yin, K. Song, C. Wang, B. Liu, M. Wu, Recent advances of NaLuF$_4$-based upconversion nanocrystals, J. Nanosci. Nanotechnol. 15 (2015) 31–40.

[13] S. Zeng, H. Wang, W. Lu, Z. Yi, L. Rao, H. Liu, J. Hao, Dual-modal upconversion fluorescent/X-ray imaging using ligand-free hexagonal phase NaLuF$_4$:Gd/Yb/Er nanorods for blood vessel visualization, Biomaterials 35 (2014) 2934–2941.

[14] M. Ding, D. Chen, C. Lu, J. Xi, Z. Ji, Z. Xu, Hydrothermal synthesis, energy transfer and luminescent properties of β-NaLuF$_4$:Ce^{3+}/Gd^{3+}/Sm^{3+} microcrystals, J. Lumin. 186 (2017) 109–116.

[15] J. Zhou, Z. Liu, F. Li, Upconversion nanophosphors for small-animal imaging, Chem. Soc. Rev. 41 (2012) 1323–1349.

[16] Q. Ju, S. Luo, C. Chen, Z. Fang, S. Gao, G. Chen, X. Chen, N. Gu, Single-irradiation simultaneous dual-modal bioimaging using nanostructure scintillators as single contrast agent, Adv. Healthcare Mater. 8 (2019) 1801324.

[17] S. Yu, D. Tu, W. Lian, J. Xu, X. Chen, Lanthanide-doped near-infrared II luminescent nanoprobes for bioapplications, Sci. China Mater. 62 (2019) 1071–1086.

[18] X. Wang, J. Shi, P. Li, S. Zheng, X. Sun, H. Zhang, LuPO$_4$:Nd^{3+} nanophosphors for dual-mode deep tissue NIR-II luminescence/CT imaging, J. Lumin. 209 (2019) 420–426.

[19] R.D. Teo, J. Termini, H.B. Gray, Lanthanides: applications in cancer diagnosis and therapy, J. Med. Chem. 59 (2016) 6012–6024.

[20] T. Sun, X. Chen, L. Jin, H.-W. Li, B. Chen, B. Fan, B. Moine, X. Qiao, X. Fan, S.-W. Tsang, S.F. Yu, F. Wang, Broadband Ce(III)-sensitized quantum cutting in core-shell nanoparticles: mechanistic investigation and photovoltaic application, J. Phys. Chem. Lett. 8 (2017) 5099–5104.

[21] C. Sun, X. Li, H. Wang, D. Xue, Crystallization-dependent luminescence properties of Ce:LuPO$_4$, Inorg. Chem. 55 (2016) 2969–2976.

[22] L. Zhao, S. Mei, W. Wang, P.K. Chu, Z. Wu, Y. Zhang, The role of sterilization in the cytocompatibility of titania nanotubes, Biomaterials 31 (2010) 2055–2063.

[23] H.K. Nagar, A.K. Srivastava, R. Srivastava, M.S. Ranawat, Evaluation of potent phytomedicine for treatment of psoriasis using UV radiation induced psoriasis in rats, Biomed. Pharmacother. 84 (2016) 1156–1162.

[24] Z. Hou, Y. Zhang, K. Deng, Y. Chen, X. Li, X. Deng, Z. Cheng, H. Lian, C. Li, J. Lin, UV-emitting upconversion-based TiO$_2$ photosensitizing nanoplatform: near-Infrared light mediated in vivo photodynamic therapy via mitochondria-involved apoptosis pathway, ACS Nano 9 (2015) 2584–2599.

[25] X.D. Ren, X.Y. Hao, H.C. Li, M.R. Ke, B.Y. Zheng, J.D. Huang, Progress in the development of nanosensitizers for X-ray-induced photodynamic therapy, Drug Discov. Today 23 (2018) 1791–1800.

[26] S. Clement, W. Deng, E. Camilleri, B.C. Wilson, E.M. Goldys, X-ray induced singlet oxygen generation by nanoparticle-photosensitizer conjugates for photodynamic therapy: determination of singlet oxygen quantum yield, Sci. Rep. 6 (2016) 19954.

[27] C. Zhang, K. Zhao, W. Bu, D. Ni, Y. Liu, J. Feng, J. Shi, Marriage of scintillator and semiconductor for synchronous radiotherapy and deep photodynamic therapy with diminished oxygen dependence, Angew. Chem. 54 (2015) 1770–1774.

[28] Z. Du, X. Zhang, Z. Guo, J. Xie, X. Dong, S. Zhu, J. Du, Z. Gu, Y. Zhao, X-ray-controlled generation of peroxynitrite based on nanosized LiLuF$_4$:Ce^{3+} scintillators and their applications for radiosensitization, Adv. Mater. 30 (2018) 1804046.

[29] X. Jiang, C. Cao, W. Feng, F. Li, Nd^{3+}-doped LiYF$_4$ nanocrystals for bio-imaging in the second near-infrared window, J. Mater. Chem. B 4 (2016) 87–95.

[30] L.S. Liu, H.H. Chen, B.Q. Liu, B. Tang, Z.J. Sun, J.T. Zhao, Microscintillator of Ce doped β-NaLuF$_4$ in uniform hexagonal prism morphology by a facile hydrothermal method, Appl. Mech. Mater. 541–542 (2014) 220–224.

[31] Z. Wang, P. Zhang, Q. Yuan, X. Xu, P. Lei, X. Liu, Y. Su, L. Dong, J. Feng, H. Zhang, Nd^{3+}-sensitized NaLuF$_4$ luminescent nanoparticles for multimodal imaging and temperature sensing under 808 nm excitation, Nanoscale 7 (2015) 17861–17870.

[32] X. Li, M. Jiang, Y. Li, Z. Xue, S. Zeng, H. Liu, 808 nm laser-triggered NIR-II emissive rare-earth nanoprobes for small tumor detection and blood vessel imaging, Mater. Sci. Eng. C 100 (2019) 260–268.

[33] F. Shi, J. Wang, X. Zhai, D. Zhao, W. Qin, Facile synthesis of β-NaLuF$_4$:Yb/Tm hexagonal nanoplates with intense ultraviolet upconversion luminescence, CrystEngComm 13 (2011) 3782–3787.

[34] X. Wang, J. Song, H. Sun, Z. Xu, J. Qiu, Multiphoton-excited upconversion luminescence of Nd:YVO$_4$, Opt. Express 15 (2007) 1384–1389.

[35] Z. Sun, Z. Fu, G. Liu, Designing down- and up-conversion dual-mode luminescence of lanthanide-doped phosphors for temperature sensing, J. Lumin. 206 (2019) 176–184.

[36] W. Fan, P. Huang, X. Chen, Overcoming the Achilles heel of photodynamic therapy, Chem. Soc. Rev. 45 (2016) 6488–6519.

[37] D. Orsi, T. Rimoldi, S. Pinelli, R. Alinovi, M. Goldoni, G. Benecchi, F. Rossi, L. Cristofolini, New CeF$_3$-ZnO nanocomposites for self-lighted photodynamic therapy that block adenocarcinoma cell life cycle, Nanomedicine 13 (2018) 2311–2326.